ADVANCED INTELLIGENT SYSTEMS Open Access
www.advintellsyst.com

Tactile Sensing and Grasping Through Thin-Shell Buckling

*Kieran Barvenik, Zachary Coogan, Gabriele Librandi, Matteo Pezzulla, and Eleonora Tubaldi**

Soft and lightweight grippers have greatly enhanced the performance of robotic manipulators in handling complex objects with varying shape, texture, and stiffness. However, the combination of universal grasping with passive sensing capabilities still presents challenges. To overcome this limitation, a fluidic soft gripper is introduced based on the buckling of soft, thin hemispherical shells. Leveraging a single fluidic pressure input, the soft gripper can grasp slippery and delicate objects while passively providing information on this physical interaction. Guided by analytical, numerical, and experimental tools, the novel grasping principle of this mechanics-based soft gripper is explored. First, the buckling behavior of a free hemisphere is characterized as a function of its geometric parameters. Inspired by the free hemisphere's two-lobe mode shape ideal for grasping purposes, it is demonstrated that the gripper can perform dexterous manipulation and gentle gripping of fragile objects in confined spaces and underwater environments. Last, the soft gripper's embedded capability of detecting contact, grasping, and release conditions during the interaction with an unknown object is proved. This simple buckling-based soft gripper opens new avenues for the design of adaptive gripper morphologies with tactile sensing capabilities for applications ranging from medical and agricultural robotics to space and underwater exploration.

1. Introduction

Shape and function in natural organisms converge toward geometries with advantageous mechanical characteristics,[1–3] leading to the formation of structural patterns across the natural world.[2] Inspired by these natural design principles, soft robots transcend the limitations of conventional rigid systems and create new possibilities for diverse functional properties. State-of-the-art soft grippers have enhanced the functionalities of robotic manipulators through precision grasping,[4,5] adaptable gripping capabilities,[6–8] fragile object manipulation,[9,10] and embedded soft sensing elements.[11,12] Additionally, soft materials enable the integration of unique properties like self-healing,[13–15] mechanical computing,[16,17] and intrinsic programmability[4,18–20] to reimagine the capabilities of robotic end effectors. Current soft grippers are designed to be actuated with a variety of stimuli, including magnetic and electric fields,[19,21,22] temperature gradients,[23,24] light energy,[25,26] and pneumatic or hydraulic inputs.[27–29]

While these actuation schemes increase the functional diversity of soft robots, they all present unique challenges ranging from slow response speed and low output force for electric, thermal, and pneumatic inputs to limited range of actuation for magnetically responsive materials, respectively. Embedding mechanical instabilities within soft devices can overcome these limitations by triggering large deformations and shape transitions in response to small changes in external stimuli.[30] Elements such as prebuckled beams,[31] multistable linkages,[32,33] or snapping doubly curved shells[34,35] have been used to produce programmable rapid reconfigurations for gripping tasks. Despite these advancements, current limitations include difficulties in enabling soft robots with multiple

K. Barvenik, Z. Coogan, E. Tubaldi
Department of Mechanical Engineering
University of Maryland
4298 Campus Dr., College Park, MD 20742, USA
E-mail: etubaldi@umd.edu

G. Librandi
Independent Researcher
Washington 20016, USA

The ORCID identification number(s) for the author(s) of this article can be found under https://doi.org/10.1002/aisy.202300855.

DOI: 10.1002/aisy.202300855

M. Pezzulla
Department of Mechanical and Production Engineering
Aarhus University
Nordre Ringgade 1, Aarhus 8000, Denmark

E. Tubaldi
Maryland Robotics Center
University of Maryland
8125 Paint Branch Dr Suite 3158, College Park, MD 20740, USA

E. Tubaldi
Robert E. Fischell Institute of Biomedical Devices
University of Maryland
8278 Paint Branch Dr Room 5102, College Park, MD 20742, USA

functional behaviors, such as fast grasping of delicate objects with a sense of touch in complex environments.

To overcome these limitations, inspiration can be once again drawn from the natural world. Among the numerous structural patterns in nature, hemisphere-like geometries appear across scales ranging from the microscale of viruses[36] and bacteria[37] to the macroscale of fungi,[38] pollen grains,[39] plants,[40] and sea creatures.[41] The folding of such hemispherical shapes represents largely observed encapsulation mechanisms among proteins and immune cells to capture sugar molecules[37] and grabs cellular debris and pathogens.[42] These patterns continue at the macroscale, where hemispherical structures facilitate diverse behaviors, from the attachment of marine leeches[43] and the adhesion of *Octopus vulgaris* suckers[44] to the locomotion of jellyfish.[45]

Megalodicopia hians, a variant of the deep-sea *Benthic tunicate*, developed large hemispherical oral siphons to catch floating organic particles. Aided by the flow of water, these oral siphons collapse around food, providing an efficient and energetically favorable feeding mechanism.[46] Here, we seek to mimic the motion of the oral siphon of the predatory deep-sea tunicate (*Ascidian, Ascidiacea*) by introducing a new class of soft, pneumatic, buckling-based hemispherical gripper (**Figure 1**A and Movie S1, Supporting Information). Deflating the hemispherical gripper triggers a lobed mode shape that resembles the predatory tunicate's siphon (Figure 1B), which can be programmed to selectively grasp, protect, and release fragile and slippery objects in unstructured and confined environments (Figure 1C), all while providing electronics-free tactile sensing.

To explore this new grasping strategy, we first demonstrate with a combination of analytical and numerical models that the free hemisphere experiences a buckling instability at a critical pressure that follows a predictable cubic trend with respect to slenderness ratio. We then combine numerical and experimental methods to investigate the behavior of the buckling-based soft inflatable gripper by applying a thin membrane on the equatorial plane of the hemisphere. We identify geometric parameters that enable constructive buckling for functional and universal grasping with a systematic exploration of the design space. Then, we show how the properties of the soft inflatable gripper can be leveraged for precise gripping and manipulation tasks of delicate objects in complex and confined environments. Last, we demonstrate that the hemispherical gripper showcases an electronics-free sense of touch while it performs dexterous grasping and manipulation tasks.

2. Results

2.1. Buckling Behavior of Free Thin-Shell Domes

The investigation of the hemispherical gripper first started with a finite element (FE) model to predict the buckling behavior of a free, thin hemispherical shell with radius R, thickness h, and cap angle θ, subjected to a uniform internal pressure P (**Figure 2**A). In the FE analyses (performed with the commercial package ABAQUS 2020/Standard), we modeled the hemisphere using four-node shell elements (S4R) and applied a neo-Hookean material model with the mechanical properties of the rubber material Elite Double 32 from Zhermack (see Section S1, Supporting Information for details). Next, we conducted buckling analyses to extract the critical buckling pressure and corresponding mode

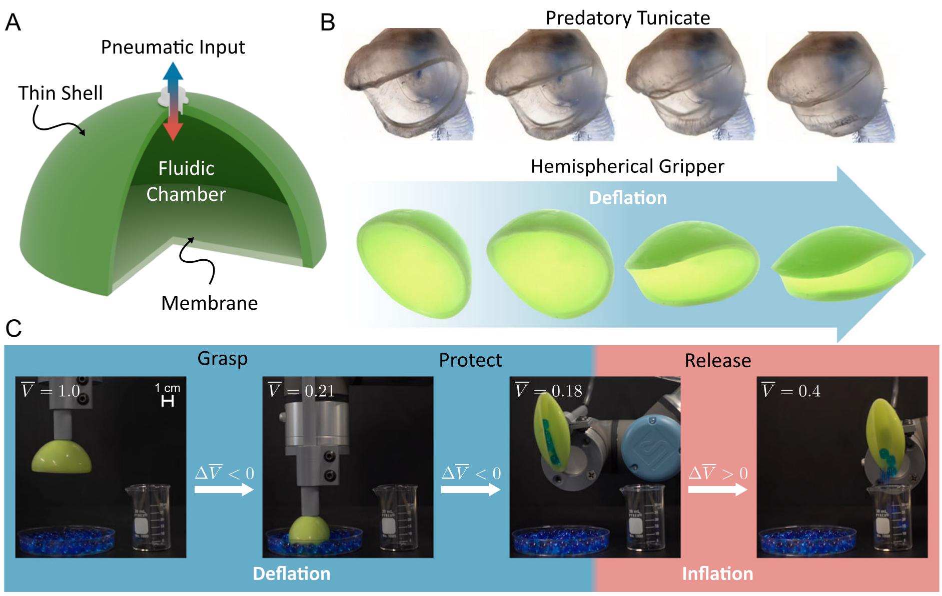

Figure 1. Function and biomimicry of the hemispherical gripper. A) Schematic of the hemispherical gripper. A fluid cavity is created within a thin hemispherical shell enclosed by an equatorial membrane. The fluid can be withdrawn or infused in the chamber through a pneumatic input at the shell's apex. B) Folding shape and feeding behavior of the predatory *Benthic tunicate* in images from *The Blue Planet* documentary.[58] Analogy with the hemispherical gripper that mimics the shape of the deep sea tunicate to gently manipulate objects. C) Experimental snapshots of the hemispherical gripper grasping, protecting, and releasing wet hydrogel spheres. The buckling-induced grasping mechanism of the hemispherical gripper based on the change in volume $\Delta\overline{V} = \Delta V/V_0$ of the fluidic cavity with initial volume V_0.

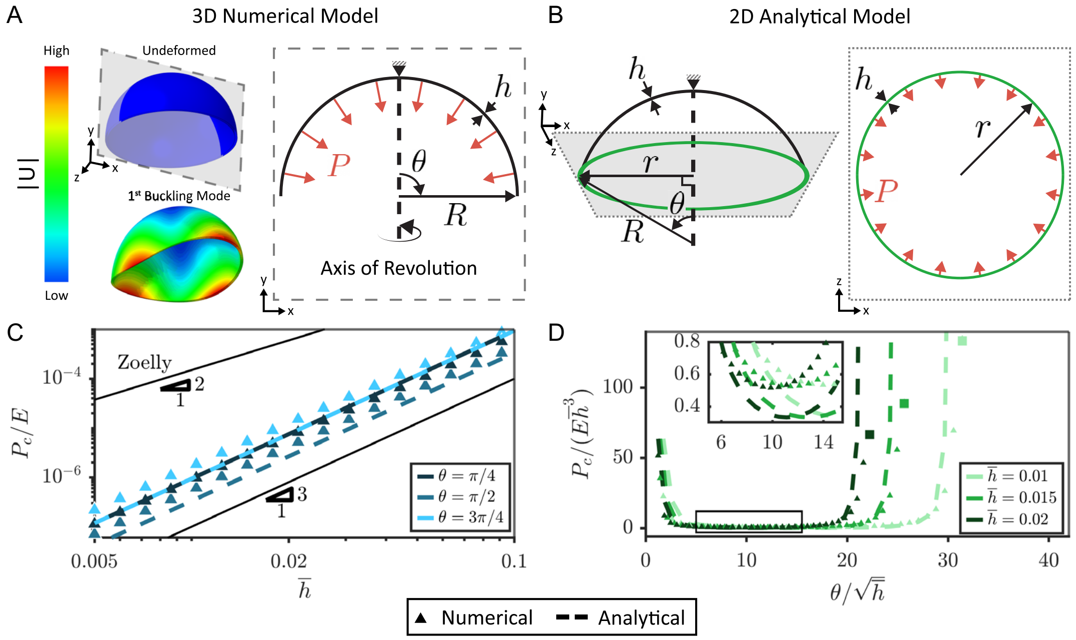

Figure 2. Buckling instability in free thin-shell domes. A) 3D numerical model: underformed shape and first buckling mode of the free hemispherical shell with radius R, thickness h, cap angle θ, and applied internal pressure P positive pointing inwards. B) Two-dimensional analytical model of the hemispherical shell based on the boundary edge of the spherical dome. C,D) Analytical and numerical results for the normalized critical buckling pressure with respect to C) slenderness ratio $\bar{h}$ and D) normalized cap angle $.\theta/\sqrt{\bar{h}}$. The squares represent the classical buckling pressure for a full sphere under uniform pressure.[48]

shape for multiple values of slenderness ratio $\bar{h} = h/R$ and cap angle θ (for more information, see Section S1 Supporting Information, for details). Based on the FE analyses, the first buckling mode exhibits a saddle shape with two pairs of upper and lower lobes, which results in the loss of rotational symmetry of the hemispherical shell (Figure 2A).

We noted that the in-plane deformation of the equatorial line of the hemispherical mode shape resembles the lobed, elliptical first mode of a circular ring.[47] Taking advantage of this observation, we developed an equivalent two-dimensional analytical model to predict the critical pressure of the rotational symmetry-breaking buckling for the hemispherical shell. Thus, we approximate the hemispherical shell with the circular ring having the properties of the equatorial line of the shell (Figure 2B). The buckling pressure of a circular ring can be written as[47]

$$P_c = \frac{E}{4(1-\nu^2)}\left(\frac{h}{r}\right)^3 \tag{1}$$

where E is the Young's modulus, ν is the Poisson's ratio, and r and h are the ring radius and thickness, respectively. In our analogy, the circular ring represents the base ring of the spherical dome with cap angle θ (Figure 2B), such that the slenderness ratio can be expressed using a projection of the hemispherical radius

$$\frac{h}{r} = \frac{h}{R}\csc\theta \tag{2}$$

By substituting Equation (2) to (1), we obtain the critical buckling pressure P_c predicted by the 2D analytical model for the spherical dome

$$P_c = \frac{E}{4(1-\nu^2)}\left(\frac{h}{R}\right)^3 \csc^3\theta \tag{3}$$

We found good agreement between the critical buckling pressures predicted from the analytical model and our FE results (Figure 2C,D). In Figure 2C, we demonstrate an observed cubic relationship between the critical buckling pressure and the slenderness ratio $\bar{h} = h/R$ for free hemispherical shells. This cubic trend differs from the classical Zoelly quadratic relationship[48] for thin-shell hemispheres with clamped boundary conditions. The lower buckling threshold observed with respect to the Zoelly theory is the result of the near-isometric deformation that the free, thin, elastic shell can reconfigure into. In Figure 2D, we report the nondimensional critical pressure $P_c/(E\bar{h}^3)$ as a function of the nondimensional cap angle $\theta/\sqrt{\bar{h}}$, and we show that both analytical and numerical results follow similar trends with a sharp increase in slope near the minimal and maximal values of the cap angle, where the geometry of the hemispherical shell approaches that of a circular plate and of a full spherical shell, respectively. The numerical results for $\theta = \pi$ also demonstrate good agreement with the classical critical buckling pressure for full spherical shells[48] (indicated by the square markers in Figure 2D).

2.2. Rational Design of the Hemispherical Gripper

Toward this goal, we explored a fully soft gripper made of a hemispherical shell with a thin film covering the equatorial plane (**Figure 3**A). The introduction of this elastic film creates an isolated fluid cavity within the dome, which enables the use of

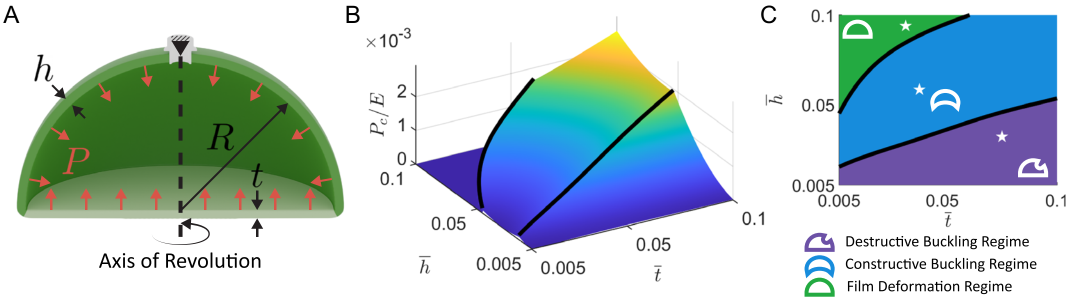

Figure 3. Numerical exploration of hemispherical shell with equatorial film. A) Schematic of the numerical model of the hemispherical gripper with radius R, shell thickness h, film thickness t, and cavity pressure P. B) Nondimensional critical buckling pressure as a function of the slenderness ratio $\bar{h}$ and normalized film thickness $\bar{t}$. The contours highlighted in black indicate where the behavior of the deflated shell transitions between deformation regimes. C) Evolution of the three behavioral regimes (i.e., "destructive" buckling, "constructive" buckling, and film deformation regime) as a function of the slenderness ratio and normalized film thickness $\bar{h}$ and $\bar{t}$, respectively. The stars indicate geometrical parameters of tested experimental samples.

pneumatic input to actuate the hemisphere. We then investigated the soft gripper's response upon deflation ($P > 0$ as shown in Figure 3A) of the internal cavity both numerically and experimentally. To study the nonlinear deformation behavior of the enclosed dome, we used the dynamic implicit solver in ABAQUS 2020/Standard for FE volume-controlled simulations by applying an incompressible fluid within the cavity (see Section S1, Supporting Information for details). The highly compliant Ecoflex 00-30 was chosen for the thin film, which we modeled using an incompressible Gent material model[49] (see the Section S1, Supporting Information for details). We explored the gripper's parameter space by fixing the cap angle $\theta = \pi/2$ and varying both the normalized film thickness $\bar{t} = t/R$ and the slenderness ratio over a range spanning $0.005 < \bar{t} < 0.1$ and $0.005 < \bar{h} < 0.1$. For each set of geometric parameters, we obtained the corresponding dome's pressure–volume deflation curve and nonlinear deformed shape, which we used to classify the structures' responses (see Section S1, Supporting Information for details).

Leveraging the numerical pressure–volume deflation curves, the critical buckling pressure of the hemispherical gripper can be determined as a function of $\bar{h}$ and $\bar{t}$ (Figure 3B). As a result, we found a nonlinear surface that includes two sharp transitions splitting the design space into three discrete regions. By examining the deformed mode shape within these regions, we classified the behavior of the soft actuator into three distinct regimes (Figure 3C): i) the "destructive" buckling regime (Regime 1), ii) the "constructive" buckling regime (Regime 2), and iii) the film deformation regime (Regime 3). The "destructive" buckling regime occurs for geometries with high film thickness and low shell thickness. In these geometries, the film stiffness outweighs the shell stiffness, such that the film acts as a fixed boundary on the shell. This boundary effect gives rise to a shell buckling response typical of soft spherical shells with clamped boundary conditions.[50,51] The "constructive" buckling regime arises when the film and shell thicknesses are comparable and both structural elements deform in unison. Here, the dome's reconfiguration closely aligns with the mode shape of the hemispherical shell with no applied film. The third regime, referred to as the film deformation regime, is governed by excessive deformation of the film surface and minimal deformation of the shell. It is found for high values of shell thickness and low values of film thickness. Inspired by our numerical findings, we experimentally validated our FE analyses by selecting three geometric configurations, one from each regime. The elastic samples were manufactured with a combination of coating[52] and mold-and-cast processes (see Section S2, Supporting Information for more details) using Zhermack Elite Double 32 and Smooth-On Ecoflex 00-30 for the hemispherical shell and the thin film, respectively. Experimental pressure–volume curves were obtained by deflating the hemispherical internal cavity using air as the working fluid and accounting for compressibility effects (see Section S3, Supporting Information for more details).

The first tested sample has slenderness ratio $\bar{h} = 0.032$ and normalized film thickness $\bar{t} = 0.076$, such that it falls within the destructive buckling regime. **Figure** 4A reports the experimental and numerical pressure–volume curves of the hemisphere, which shows the classic sudden drop in pressure that corresponds to the catastrophic buckling onset for $|\Delta V/V_0 = 0.455|$. This traditional, catastrophic shell buckling response does not produce a mode shape conducive for grasping, and instead suddenly forms a dimple that asymmetrically angles the hemisphere away from its resting configuration (Figure 4D and Movie S2, Supporting Information) Thus, in the context of grasping, this regime produces nonfunctional, or "destructive," buckling behavior.

The second tested hemisphere has slenderness ratio $\bar{h} = 0.058$ and normalized film thickness $\bar{t} = 0.040$, putting it in the constructive buckling regime. In Figure 4, the predicted FE pressure–volume curve of the hemisphere shows a sudden change in slope at the onset of the rotational symmetry-breaking buckling for $|\Delta V/V_0 = 0.435|$. By triggering this deformation which pinches together the two lobes on the minor axis (Figure 4E and Movie S2, Supporting Information), the shell's response facilitates secure grasping. Given these lobed mode shape, the shells in this regime are the most functional for manipulation tasks, so we classify them as undergoing "constructive" buckling.

Our third hemispherical sample has slenderness ratio $\bar{h} = 0.094$ and normalized film thickness $\bar{t} = 0.034$ and falls within the film deformation regime. In Figure 4C, the numerical pressure–volume curve of the hemisphere presents a fairly linear

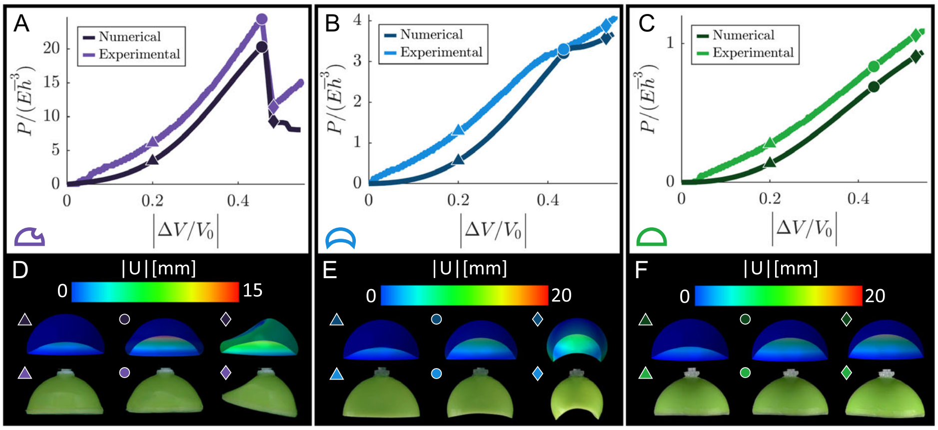

Figure 4. Modeling and Experimental Validation. A–C) Numerical and experimental comparison of the normalized pressure–volume curves for hemispherical shells in Regime 1 ($\bar{h} = 0.032$, $\bar{t} = 0.076$), Regime 2 ($\bar{h} = 0.058$, $\bar{t} = 0.040$), and Regime 3 ($\bar{h} = 0.094$, $\bar{t} = 0.034$), respectively. D–F) Snapshots of the numerical and experimental deformed shapes in Regime 1, Regime 2, and Regime 3, respectively, highlighted by the markers in the corresponding pressure-volume curves. The numerical results include a transparency applied to the hemispherical shell to enable visualization of the film deformation.

trend without any appearance of a buckling instability. Similarly to the "destructive" buckling regime, domes that fall within the film deformation regime do not produce a significant deformation of the equatorial line to be harnessed to grasping tasks (Figure 4F and Movie S2, Supporting Information). These observations about the grasping effectiveness of each regime reduce the design space of hemispherical grippers to the "constructive" buckling region bounded in blue in Figure 3C.

2.3. Grasping with a Sense of Touch

Given the constructive buckling regime ideal for grasping tasks, we then sought to examine the grasping performance of the gripper with embedded sensing capabilities. Due to the deformable nature of the gripper design, collisions with external objects change the shape and volume of the gripper, creating measurable differences in the operating fluid pressure.[53] Specifically, we explore how the geometry of the hemispherical gripper uniquely enhances the ability to discern environmental stimuli based on the simple pressure response.

To test the hemispherical gripper's sensing capabilities, we connected the hemispherical gripper ($\bar{h} = 0.052$ and $\bar{t} = 0.048$) and the pneumatic system to a commercial robotic arm to precisely and reliably control the motion of the soft actuator. The hemispherical gripper is used to grasp a series of cylinders with diameters $d_{\text{cyl,A}} = 10\,\text{mm}$, $d_{\text{cyl,B}} = 20\,\text{mm}$, and $d_{\text{cyl,C}} = 30\,\text{mm}$ and the resulting pressure-volume curves are compared to a reference curve, which corresponds to a trial of the gripper's deformation without grasping an object (**Figure 5**). Figure 5A highlights the deflation response of the gripper, during which the actuator first makes contact with the object and then, through the two-lobed mode shape, grasps the object via pinching. The downward spike at $|\Delta V/V_0 \simeq 0.035|$ occurs when the gripper contacts the object, which is labeled as I. This contact deforms the gripper's membrane inwards, which suddenly shrinks the internal volume of the gripper causing a jump in fluid pressure (the jump is downward due to the previously defined sign convention for fluid pressure).

Similarly, the moment that the object is pinched by the gripper's lobes can be identified in Figure 5A as point II corresponding to $|\Delta V/V_0 = 0.636|$ for $d_{\text{cyl,A}} = 10\,\text{mm}$, $|\Delta V/V_0 = 0.565|$ for $d_{\text{cyl,B}} = 20\,\text{mm}$, and $|\Delta V/V_0 = 0.484|$ for $d_{\text{cyl,C}} = 30\,\text{mm}$. Here, a further inward deflection of the gripper's lobes is restricted by the contact with the grasped object. The constraint imposed by the presence of the object causes the pressure to increase more sharply with respect to the reference case (i.e., without object). A similar pattern can be used to detect the moment the gripper releases the object, which is highlighted as III in Figure 5B. When the object is released ($|\Delta V/V_0 = 0.594|$ for $d_{\text{cyl,A}} = 10\,\text{mm}$, $|\Delta V/V_0 = 0.529|$ for $d_{\text{cyl,B}} = 20\,\text{mm}$, and $|\Delta V/V_0 = 0.447|$ for $d_{\text{cyl,C}} = 30\,\text{mm}$), the constraint causing a relative increase in fluid pressure disappears, causing the trial curves to collapse back onto the reference curve. These sensing events—contact, grasp, and release—can be detected without introducing any external sensing elements, and each stimulus scales with the properties of the object to reveal information about its size and shape (see Movie S3, Supporting Information). The sensitivity of the gripper can be characterized by monitoring the fluid pressure within the gripper as indenters of varying diameters are plunged into its thin film (see Section S3, Supporting Information for details). The slope of the resulting pressure–displacement plot, which reflects how the fluid pressure responds to incremental indentations, yields a measure of the gripper's contact sensitivity s that is found to be $0.175\,\text{kPa}\,\text{mm}^{-1}$ (see Section S3, Supporting Information for details). This sensitivity value is compared to the sensitivities of other pneumatic gripper and actuator designs in **Figure 6**. Here, we observe that the hemispherical gripper outperforms the other gripper designs, having almost twice the sensitivity of the next highest (the commercial vacuum gripper, with $s = 0.09\,\text{kPa}\,\text{mm}^{-1}$). This observation aligns with the unique design of the hemispherical gripper: because the gripper's lowest stiffness component, its thin film, is in contact with the objects,

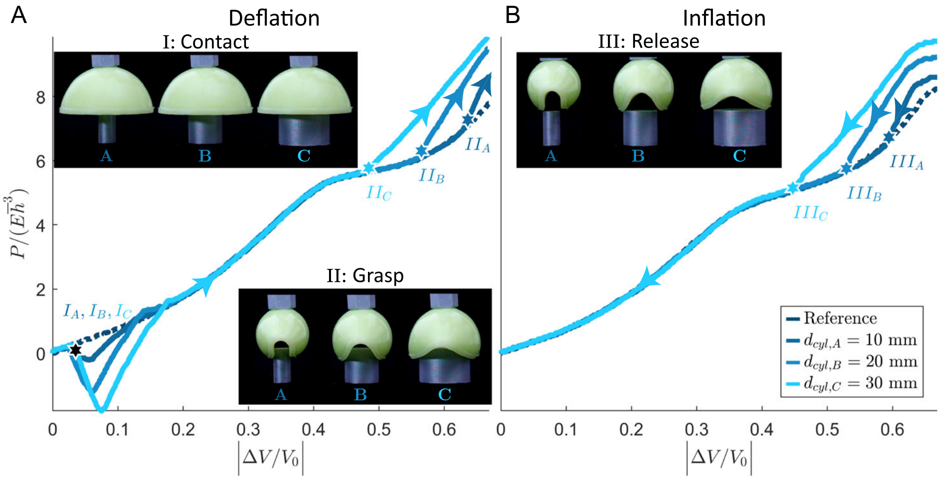

Figure 5. Embedded sensing capabilities. A) Deflation curves of a hemispherical gripper ($\bar{h} = 0.052$ and $\bar{t} = 0.048$) grasping cylinders of three different diameters. The pressure–volume response for each cylinder trial is overlaid with a reference curve, which showcases the deflation response of the gripper without a grasped object. By comparing the trial curves to the reference curve, interactions with the environment, including contact I) and the onset of grasping II) can be detected. The stars on the deflation curves highlight the points at which the inset images were recorded. B) Inflation curves for the grasping trials. By comparing the trial curves to the reference curve and monitoring when they converge, the moment the object is released can be determined (III).

Label	Name	Sensing Task
	Hemispherical Gripper	Contacting circular indenters, diameter 10 to 40 mm
	Vacuum Gripper [54]	Grasping cylindrical objects, diameter 30 to 70 mm
	Commercial PneuNet Gripper [54]	Grasping cylindrical objects, diameter 40 to 100 mm
	PneuNet Gripper [54]	Grasping cylindrical objects, diameter 40 to 100 mm
	TPU Bending Actuator [54]	Wrapping around cylindrical objects, diameter 60 to 100 mm
	PneuNet Actuator [54]	Detecting distance to flat plate, ranging from 0 to 40 mm

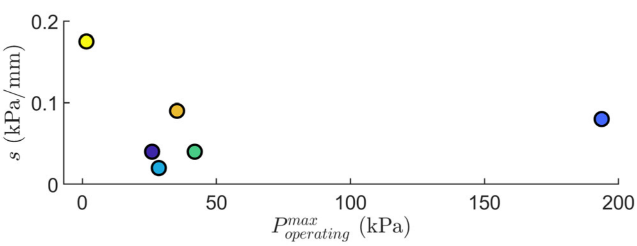

Figure 6. Comparison of grippers sensitivity performance. Comparison of the hemispherical gripper's average sensitivity and maximum operating pressure relative to other pneumatic gripper designs. Data for all other compared designs are tabulated within.[53]

the gripper is more sensitive to pressure perturbation resulting by the interaction with external objects. This is in contrast to many classical pneumatic bending actuators where stiffer elements are placed in contact with the objects to enable their bending motion. Additionally, the hemispherical gripper has the lowest operating pressure compared to the other grippers, with only 1.5 kPa required to yield its grasping deformation. This attribute makes the gripper simple and affordable to control, while also providing potential important safety benefits in delicate environments.

2.4. Object Manipulation in Complex Environments

After exploring the sensitivity of the hemispherical gripper and benchmarking it against state-of-the-art pneumatic grippers, we sought to uncover how it performed grasping objects with varying sizes, shapes, and stiffnesses. **Figure 7**A–D shows the soft gripper ($\bar{h} = 0.052$, $\bar{t} = 0.048$) grasping and releasing a piece of gelatin, a cube of tofu, a raspberry, and a screwdriver, respectively, which vary strongly in size, shape, stiffness, and fragility. The versatility of the hemispherical gripper is also demonstrated by the grasping of multiple different objects in Movie S4, Supporting Information. Similarly to Figure 5, we collected baseline pressure–volume curves from the gripper without grasping an object. These reference curves were then overlapped with the experimental curves of the gripper recorded while performing a grasping task. By highlighting differences between the reference and experimental responses like we observe in Figure 5, we can locate the contact, grasp, and release points that characterize the interaction of the gripper with the grasped object in real time (see Section S3, Supporting Information for details). Though the responses are similar, we can observe certain qualititative differences such as the relatively small contact jump imposed by the low stiffness piece of gelatin in Figure 7A. Additionally, the contact-induced jump that occurs after the onset of buckling at $|\Delta V/V_0 \simeq 0.42|$ in Figure 7D shows how the sensing events are discernible regardless of when they occur during deflation.

The gripper's extreme versatility and compliance also enable a wider range of operations such as grasping objects underwater

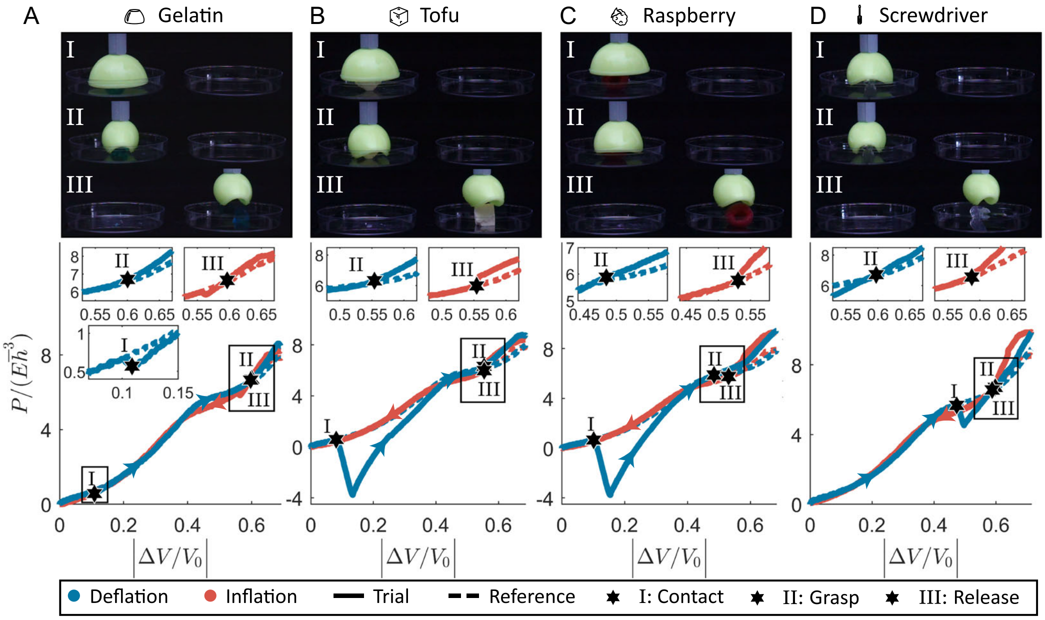

Figure 7. Experimental grasping trials. A–D) Experimental snapshots and normalized pressure–volume curves of the hemispherical gripper ($\bar{h} = 0.052$ and $\bar{t} = 0.048$) grasping a piece of gelatin, a cube of tofu, a raspberry, and a screwdriver, respectively. The dashed lines represent the response of the gripper without grasping an object. I) Contact, II) buckling, and III) release key points are labeled in all the experimental curves.

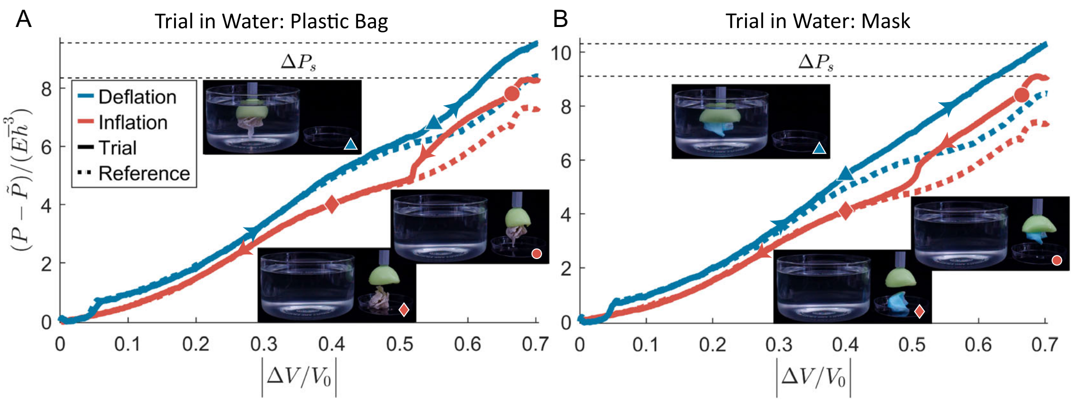

Figure 8. Underwater Grasping Trials. A,B) Experimental snapshots and normalized pressure–volume curves of the hemispherical gripper grasping a plastic bag and a mask, respectively, while submerged in water. In both trials, water is used as the operating fluid within the hemisphere rather than air. To compensate for the pressure head changes induced by the motion of the robotic arm, the pressure head $\tilde{P} = \rho_{H_2O}gz$ is subtracted from the measured pressure values, where z represents the change in height of the robot arm relative to its initial height. The difference between the gripper deflating while submerged in water while reinflating outside of water also leads to the maximum pressure difference $\Delta P_s = \tilde{P}_{def} - \tilde{P}_{inf}$. The markers highlight the points in the pressure–volume curves corresponding to the snapshots in the insets.

and in confined environments. **Figure** 8A,B and Movie S5, Supporting Information, highlight the gripper being used to remove litter in the form of a plastic bag and a mask, respectively, from a small body of water. For these trials, the fluid within the hemisphere was replaced by water, and the litter items were grasped underwater and extracted outside the water to a separate location. Since, when using water as the operating fluid, the height of the robotic arm impacts the pressure within the system, the initial value of the pressure $\tilde{P}$ corresponding to the initial pressure head induced by the change in height is subtracted from the pressure values. Though the gripper responds similarly when within or outside of water, there is a pressure drop ΔP_s between the deflation and inflation curves that arises when the fluid surrounding the hemisphere changes from water, when submerged, to air.

Figure 9 depicts the gripper being used to perform a grasping task through a constrained opening in a rigid plate. The gripper is deflated to fit within the confined space and is then reinflated to perform the grasping task. Once the task is completed, the gripper is deflated once again to be removed from the confined

ADVANCED INTELLIGENT SYSTEMS Open Access
www.advintellsyst.com

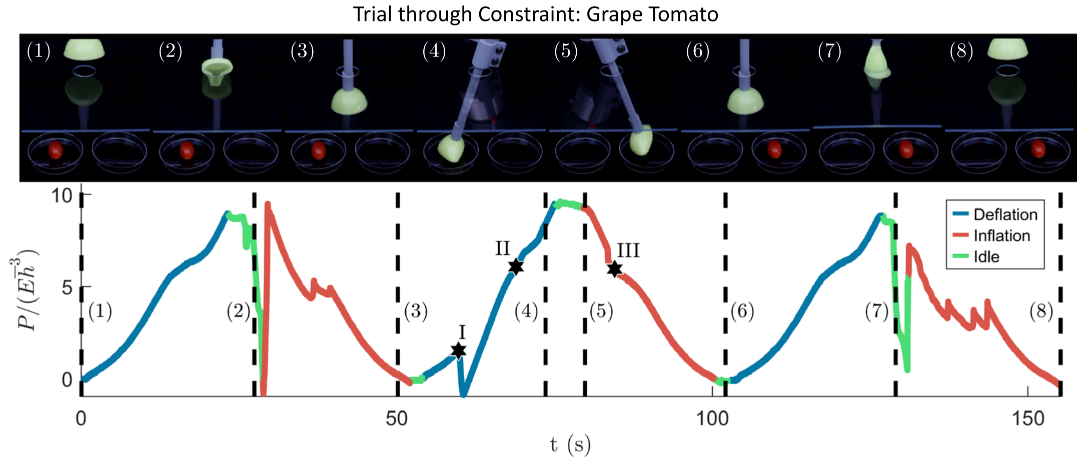

Figure 9. Grasping Through a Constraint. Experimental snapshots and normalized pressure–time response of the hemispherical gripper operating through a constrained opening to manipulate a cherry tomato. I) Contact, II) buckling, and III) release key points are labeled in the experimental curve.

space, where it can be reinflated back to its initial configuration. Through the pressure measurements recorded during the deflation, idle, and inflation phases, we can identify the interactions of the hemispherical gripper not only with the grasped objects but also with the surrounding environment. The pressure curve gives the opportunity to classify of the contact, grasping, and release points with the object, as well as to identify its passage through the confined opening. Indeed, during the idle phase, a large spike is observed when the soft gripper is inserted into ($t = 26.9$ s) and removed from ($t = 128.7$ s) the tiny hole, respectively. During insertion, the pressure spike is deeper because the motion is opposite to the natural curvature of the soft gripping shell. However, the spike is smaller when the soft gripper is being removed, since it can fold more easily into a smaller diameter shape. The response during this constrained experiment can be found in Movie S6, Supporting Information.

3. Conclusions

In summary, we have introduced a novel class of hemispherical gripper capable of manipulating fragile, slippery, and deformable bodies, while simultaneously providing a simple, embedded, responsive electronics-free sensing strategy. Enabled by a buckling instability, this gripper reconfigures rapidly into a two-node mode shape ideal for grasping and encapsulating objects even within narrow and confined environments. We investigated the design principles that can guide the development of grippers that demonstrate this buckling phenomenon, which we harnessed to manipulate objects ranging in fragility, size, and shape. The resulting large amplitude reconfigurations of the device enable it to perform complex grasping tasks after being forced through openings smaller than the size of the gripper itself. Since the buckling instability is scale independent, the hemispherical gripper's grasping behavior, here demonstrated at the centimeter scale, creates opportunities to develop large or micro scale grippers based on the same fundamental principles.

The inherent simplicity of the design enables to collect nuanced sensing information purely by monitoring the pressure–volume response of the soft gripper while interacting with the grasped objects and the confined surrounding environment. Contact, buckling, and release key points appear as discernible inflection points in the pressure–volume collected data, and they can be located real time. This data processing is performed in real time, creating countless opportunities to utilize the device in constrained, extreme, and low visibility environments without the need for additional sensing components. These features combine to yield a simple, comprehensive solution to universal grasping that includes the embedded sensing capability to extract meaningful information about live interactions across any physical scale.

Variations of the proposed design can integrate remote control using stimuli-responsive materials,[54] such as liquid crystal elastomer shells[55] and magneto-active elastic shells.[56] Localized shell imperfections[50] can also be seeded and harnessed to tune the hemispherical shell buckling onset and preprogram the gripper response. We anticipate that this highly responsive and scalable soft gripper will set a new path for the next-generation haptic devices and soft robots with electronics-free sense of touch designed to operate in unpredictable environments.[57]

4. Experimental Section

Rigorous descriptions of the methodology used for each step of our investigation are provided within the Supplementary Materials. The design of the hemispherical grippers and the manufacturing process we utilized are described in Section S1, Supporting Information. Section S2, Supporting Information details the experimental setup we utilized, the steps we took to account for compressibility, a discussion of the gripper's payload-to-weight ratio, and the methodology we adopted to label key points from pressure data. Parameters used for the finite element method investigations and the process we leveraged to categorize shells within our design space are explored in Section S3, Supporting Information.

Supporting Information

Supporting Information is available from the Wiley Online Library or from the author.

Acknowledgements

The authors gratefully acknowledge the support of the Maryland Robotics Center (MRC) as well as the Robotics Manipulator Lab at UMD. E.T. was supported by funding from the University of Maryland Start-up Package. K.B. was supported by funding from the Maryland Robotics Center Pathway to PhD program as well as the Clark Doctoral Fellowship from the University of Maryland.

Conflict of Interest

The authors declare no conflict of interest.

Author Contributions

E.T., M.P., and G.L.: proposed the research concept. K.B.: conducted modeling and numerical simulations. Z.C.: manufactured all experimental samples. K.B. and Z.C.: conducted experimental work. K.B. and E.T.: analyzed the data and wrote the paper. All co-authors revised the paper. E.T.: supervised and coordinated the research.

Data Availability Statement

The data that support the findings of this study are available from the corresponding author upon reasonable request.

Keywords

buckling, soft gripper, thin shell

Received: December 8, 2023
Revised: April 5, 2024
Published online:

[1] D'Arcy W. Thompson, in *On Growth and Form* (Ed: J. T. Bonner), 1st ed., Cambridge University Press, Cambridge, England.
[2] P. Ball, in *Nature's Patterns: A Tapestry in Three Parts*, Oxford University Press, Oxford, UK OCLC: ocn729742295.
[3] J. R. Banavar, T. J. Cooke, A. Rinaldo, A. Maritan, *Proc. Nat. Acad. Sci.* **2014**, *111*, 3332.
[4] Y. Yang, K. Vella, D. P. Holmes, *Sci. Robot.* **2021**, *6*, eabd6426.
[5] Y. Hong, Y. Chi, S. Wu, Y. Li, Y. Zhu, J. Yin, *Nat. Commun.* **2022**, *13*, 530.
[6] E. Brown, N. Rodenberg, J. Amend, A. Mozeika, E. Steltz, M. R. Zakin, H. Lipson, H. M. Jaeger, *Proc. Nat. Acad. Sci.* **2021**, *107*, 18809–18814.
[7] S. Li, J. J. Stampfli, H. J. Xu, E. Malkin, E. V. Diaz, D. Rus, R. J. Wood, in *2019 International Conference on Robotics and Automation (ICRA)*, IEEE, Piscataway, NJ pp. 7401–7408.
[8] K. Becker, C. Teeple, N. Charles, Y. Jung, D. Baum, J. C. Weaver, L. Mahadevan, R. Wood, *Proc. Nat. Acad. Sci.* **2022**, *119*, e2209819119.
[9] N. R. Sinatra, C. B. Teeple, D. M. Vogt, K. K. Parker, D. F. Gruber, R. J. Wood, *Sci. Robot.* **2019**, *4*, eaax5425.
[10] Z. Yoder, D. Macari, G. Kleinwaks, I. Schmidt, E. Acome, C. Keplinger, *Adv. Funct. Mater.* **2023**, *33*, 2209080.
[11] R. L. Truby, M. Wehner, A. K. Grosskopf, D. M. Vogt, S. G. M. Uzel, R. J. Wood, J. A. Lewis, *Adv. Mater.* **2018**, *30*, 1706383.
[12] M. S. Li, T. M. Huh, C. R. Yahnker, H. S. Stuart, *IEEE Robot. Autom. Lett.* **2022**, *7*, 10105.
[13] E. Acome, S. K. Mitchell, T. G. Morrissey, M. B. Emmett, C. Benjamin, M. King, M. Radakovitz, C. Keplinger, *Science* **2018**, *359*, 61.
[14] Z. Liu, Y. Wang, Y. Ren, G. Jin, C. Zhang, W. Chen, F. Yan, *Mater. Horiz.* **2020**, *7*, 919.
[15] S. Terryn, J. Brancart, D. Lefeber, G. V. Assche, B. Vanderborght, *Sci. Robot.* **2017**, *2*, eaan4268.
[16] H. Yasuda, P. R. Buskohl, A. Gillman, T. D. Murphey, S. Stepney, R. A. Vaia, J. R. Raney, *Nature* **2021**, *598*, 39.
[17] Z. Lin, Z. Wang, W. Zhao, Y. Xu, X. Wang, T. Zhang, Z. Sun, L. Lin, Z. Peng, *Adv. Intell. Syst.* **2023**, *5*, 2200329.
[18] S. Zhuo, Z. Zhao, Z. Xie, Y. Hao, Y. Xu, T. Zhao, H. Li, E. M. Knubben, L. Wen, L. Jiang, M. Liu, *Sci. Adv.* **2020**, *6*, eaax1464.
[19] Q. Ze, X. Kuang, S. Wu, J. Wong, S. M. Montgomery, R. Zhang, J. M. Kovitz, F. Yang, H. J. Qi, R. Zhao, *Adv. Mater.* **2020**, *32*, 1906657.
[20] C. Wang, K. Sim, J. Chen, H. Kim, Z. Rao, Y. Li, W. Chen, J. Song, R. Verduzco, C. Yu, *Adv. Mater.* **2018**, *30*, 1706695.
[21] Z. Zhang, X. Li, X. Yu, H. Chai, Y. Li, H. Wu, S. Jiang, *Compos. Struct.* **2019**, *229*, 111422.
[22] Y. Alapan, A. C. Karacakol, S. N. Guzelhan, I. Isik, M. Sitti, *Sci. Adv.* **2020**, *6*, eabc6414.
[23] Y. Cheng, K. Ren, D. Yang, J. Wei, *Sens. Actuators. B Chem.* **2018**, *255*, 3117.
[24] J. C. Breger, C. K. Yoon, R. Xiao, H. R. Kwag, M. O. Wang, J. P. Fisher, T. D. Nguyen, D. H. Gracias, *ACS Appl. Mater. Interfaces* **2015**, *7*, 3398.
[25] M. P. D. Cunha, Y. Foelen, R. J. H. Raak, J. N. Murphy, T. A. P. Engels, M. G. Debije, A. P. H. J. Schenning, *Adv. Opt. Mater.* **2019**, *7*, 1801643.
[26] X. Pan, N. Grossiord, J. A. H. P. Sol, M. G. Debije, A. P. H. J. Schenning, *Adv. Funct. Mater.* **2021**, *31*, 2100465.
[27] F. Ilievski, A. D. Mazzeo, R. F. Shepherd, X. Chen, G. M. Whitesides, *Angew. Chem. Int. Ed.* **2011**, *50*, 1890.
[28] S. Li, D. M. Vogt, D. Rus, R. J. Wood, *Proc. Nat. Acad. Sci.* **2017**, *114*, 13132.
[29] R. Deimel, O. Brock, *Int. J. Robot. Res.* **2016**, *35*, 161.
[30] A. Pal, V. Restrepo, D. Goswami, R. V. Martinez, *Adv.Mater* **2021**, *33*, 2006939.
[31] D. Yang, B. Mosadegh, A. Ainla, B. Lee, F. Khashai, Z. Suo, K. Bertoldi, G. M. Whitesides, *Adv. Mater.* **2015**, *27*, 6323.
[32] Y. Tang, Y. Chi, J. Sun, T.-H. Huang, O. H. Maghsoudi, A. Spence, J. Zhao, H. Su, J. Yin, *Sci. Adv.* **2020**, *6*, eaaz6912.
[33] Y. Lin, C. Zhang, W. Tang, Z. Jiao, J. Wang, W. Wang, Y. Zhong, P. Zhu, Y. Hu, H. Yang, J. Zou, *Adv. Sci.* **2021**, *8*, 2102539.
[34] Q. Qi, C. Xiang, V. A. Ho, J. Rossiter, *Soft Robot.* **2022**, *9*, 1040.
[35] L. Jin, Y. Yang, B. O. Torres Maldonado, S. D. Lee, N. Figueroa, R. J. Full, S. Yang, *Adv. Intell. Syst.* **2023**, *5*, 2300039.
[36] J. Lidmar, L. Mirny, D. R. Nelson, *Phys. Rev. E* **2003**, *68*, 051910.
[37] J. Glaenzer, M. F. Peter, G. H. Thomas, G. Hagelueken, *Biophys. J.* **2017**, *112*, 109.
[38] E. Schaechter, *Nature* **2002**, *419*, 253.
[39] E. Katifori, S. Alben, E. Cerda, D. R. Nelson, J. Dumais, *Proc. Nat. Acad. Sci.* **2010**, *107*, 7635.
[40] Y. Forterre, J. M. Skotheim, J. Dumais, L. Mahadevan, *Nature* **2005**, *433*, 421.
[41] D. Nakane, M. Miyata, *Proc. Nat. Acad. Sci.* **2007**, *104*, 19518.
[42] S. Tauzin, T. W. Starnes, F. B. Becker, P.-Y. Lam, A. Huttenlocher, *J. Cell Biol.* **2014**, *207*, 589.
[43] E. M. Burreson, *Invertebr. Syst.* **2020**, *34*, 235.
[44] F. Tramacere, A. Kovalev, T. Kleinteich, S. N. Gorb, B. Mazzolai, *J. R. Soc. Interface* **2014**, *11*, 20130816.

[45] J. H. Costello, S. P. Colin, J. O. Dabiri, B. J. Gemmell, K. N. Lucas, K. R. Sutherland, *Annu. Rev. Mar. Sci.* **2021**, *13*, 375.
[46] J. D. Gage, P. A. Tyler, in *Deep-Sea Biology: A Natural History of Organisms at the Deep-Sea Floor Reprint with Corrections*, Universities Press **1999**.
[47] S. Timoshenko, J. M. Gere, *Theory of Elastic Stability* 2nd ed., Dover Publications, Mineola, NY **2009**, OCLC: ocn294885242.
[48] R. Zoelly, *Ueber ein Knickungsproblem an der Kugelschale, Thesis*, ETH Zurich **1915**.
[49] A. N. Gent, *Rubber Chem. Technol.* **1996**, *69*, 59.
[50] A. Lee, F. L. Jiménez, J. Marthelot, J. W. Hutchinson, P. M. Reis, *J. Appl. Mech.* **2016**, *83*, 111005.
[51] J. W. Hutchinson, J. Michael, T. Thompson, *Philos. Trans. R. Soc. A* **2017**, *375*, 20160154.
[52] A. Lee, P.-T. Brun, J. Marthelot, G. Balestra, F. Gallaire, P. M. Reis, *Nat. Commun.* **2016**, *7*, 11155.
[53] S. Zou, S. Picella, J. D. Vries, V. G. Kortman, A. Sakes, J. T. B. Overvelde, *Nat. Commun.* **2024**, *15*, 539.
[54] J.-H. Lee, H. S. Park, D. P. Holmes, *Math. Mech. Solids* **2021**, 10812865231159676.
[55] V. S. R. Jampani, R. H. Volpe, K. R. de Sousa, J. F. Machado, C. M. Yakacki, J. P. F. Lagerwall, *Sci. Adv.* **2019**, *5*, eaaw2476.
[56] D. Yan, M. Pezzulla, L. Cruveiller, A. Abbasi, P. M. Reis, *Nat. Commun.* **2021**, *12*, 2831.
[57] R. W. Ogden, *Non-Linear Elastic Deformations*, Courier Corporation, North Chelmsford, MA **1997**.
[58] A. Fothergill, *Blue Planet: The Deep* **2001**.

